



Microstructure evolution and mechanical properties of Ti-15-3 alloy joint fabricated by submerged friction stir welding

Peng Han¹ · Kuaishe Wang¹ · Wen Wang¹ · Lijin Ni¹ · Jia Lin¹ · Yating Xiang¹ · Qiang Liu¹ · Ke Qiao¹ · Fengming Qiang¹ · Jun Cai¹

Received: 25 October 2023 / Revised: 22 December 2023 / Accepted: 11 January 2024 / Published online: 8 February 2024
© Wroclaw University of Science and Technology 2024

Abstract

In this work, the Ti-15-3 alloy joints were successfully prepared via submerged friction stir welding (SFSW) for the first time. The microstructure evolutions and mechanical properties of the SFSW joints were characterized by electron backscattering diffraction, finite element simulation, microhardness, and tensile tests. The results revealed that the joint included three distinct zones, named as stirring zone (SZ), thermo-mechanically affected zone (TMAZ), and base metal (BM), respectively. During SFSW, the peak temperature (~808 °C) and strain in SZ gradually decreased from the upper surface to the bottom surface along the thickness of the as-received plate. Meanwhile, the temperature and strain on the advancing side (AS) were higher than that of the retreating side (RS) within SZ. Comparatively, a slightly low temperature (~480 °C) and strain occurred in TMAZ. Due to the high temperature and large strain during SFSW, the grains were significantly refined, and the major grain refinement mechanism of SZ was continuous dynamic recrystallization, while that of TMAZ was coupled by continuous and discontinuous dynamic recrystallization. Note that the ideal shear texture formed in SZ. The shear texture components at the top, center, and bottom of SZ center were $D_2(1\bar{1}\bar{2})[111]$, while that of AS and RS within SZ was $D_1(1\bar{1}\bar{2})[111]$. Finally, the ultimate tensile strengths of SZ and TMAZ were 854 MPa and 816 MPa, which reached that of 103% and 96% of BM, respectively. In summary, it was an effective method to prepare a uniform and high-performance Ti-15-3 alloy joint through SFSW.

Keywords Submerged friction stir welding · Titanium · Microstructure · Dynamic recrystallization · Finite element simulation

1 Introduction

Titanium (Ti) alloys have been extensively used in aerospace, deep-sea exploration and biomedical fields due to their low density, high specific strength, good corrosion resistance as well as excellent biocompatibility [1]. Among them, as a metastable β -type Ti alloy, Ti-15V-3Cr-3Al-3Sn (Ti-15-3) alloy, shows excellent cold formability and heat

treatment properties. Hence the Ti-15-3 alloy receives wide attention from researchers [2]. In the application process, the welding of Ti-15-3 alloy is essential [3]. Traditional fusion welding technologies exhibit some problems, i.e., high heat input, coarse grains in the nugget zone, high residual stress of the joints, and frequently occurring solidification defects such as pores and cracks. Especially for Ti-15-3 alloy, element and phase segregation are easy to occur during fusion welding, which seriously deteriorates the mechanical properties of weld joints [4].

Friction stir welding (FSW) is invented by The Welding Institute in 1991. It is a solid-state process in which metallurgical bonding is produced at temperatures below the melting point [5]. During the FSW process, the materials of the stirring zone (SZ) can be significantly refined, densified, and homogenized by severe plastic deformation [6]. At present, FSW has been extensively used for low-melting materials such as magnesium [6] and aluminum alloys [7], while

✉ Kuaishe Wang
wangkuaishe888@126.com

✉ Wen Wang
wangwen2025@126.com

¹ School of Metallurgical Engineering, National and Local Joint Engineering Research Center for Functional Materials Processing, Xi'an University of Architecture and Technology, No. 13 Yanta Road, Xi'an 710055, Shaanxi, People's Republic of China

there are still many problems to be studied in high-melting materials such as titanium [8], steel [9], and zirconium [10]. Pouraliakbar et al. [11] pointed out that the welding parameters determine the heat input during FSW, which affects the microstructure and mechanical properties of the welded joint. They found the heat input during FSW is proportional to the rotation speed of the stirring tool and inversely proportional to the welding speed. Zhang et al. [12] found that when the peak temperature exceeds β -transus temperature of Ti alloy, the SZ is mainly composed of lamellar $\alpha + \beta$ microstructure, and with the decrease of heat input, the mechanical properties of FSW joints are improved. Kitamura et al. [13] and Su et al. [14] showed that when the peak temperature is lower than β -transus temperature, SZ is mainly made up of fine equiaxed α phase, and the mechanical properties of the joint are better than that of the FSW joint whose peak temperature exceeds the β -transus temperature. Therefore, the optimized FSW parameters can contribute to obtaining fine equiaxed microstructure, thus improving the mechanical properties of FSW Ti alloy joints.

At present, in addition to optimizing the FSW parameters, the heat input can also be reduced by the cooling medium such as water [15], liquid CO₂ [16] and liquid nitrogen [17]. Therefore, the submerged friction stir welding (SFSW) technology is proposed. SFSW is originally applied to weld aluminum alloys, which effectively improves the dissolution and coarsening of precipitates in the heat-affected zone (HAZ) and thermo-mechanically affected zone (TMAZ) of the joints, thus fabricating the fine/ultrafine-grained aluminum alloys [15]. Recently, SFSW has been gradually applied to weld the pure Ti and TC4 Ti alloy by Wu et al. [18, 19]. Usually, dynamic recrystallization (DRX) easily occurs in SZ and TMAZ due to the high temperature and high strain rates during FSW/SFSW Ti alloys, thus significantly refining the grains. Kim et al. [20] believed that the major grain refinement mechanism in SZ was continuous dynamic recrystallization (CDRX) during FSW TC4 Ti alloy. Singh et al. [21] demonstrated that the grains were refined obviously due to the combination of various DRX mechanisms during FSW pure Ti. Moreover, they thought the CDRX and twinning-induced DRX occurred in the recovery stage and early stage of deformation, while the geometric dynamic recrystallization (GDRX) and discontinuous dynamic recrystallization (DDRX) appeared in the late stage of deformation. Similarly, Wu et al. [18] reported that the grain refinement mechanism in SZ was mainly controlled by twinning, prismatic slip, and basal slip at the initial stage of deformation for SFSW pure Ti joints. With the increase in temperature, the deformation mode turned to prismatic slip, and the grain refinement mechanism turned to CDRX and DDRX. In addition, Mironov et al. [22] prepared the Ti-15-3 alloy joints via FSW, and their results showed that SZ and TMAZ were dominated by DDRX and CDRX, respectively,

and ideal shear textures were formed around the pin. Similar results were also reported by Liu et al. [23]. In summary, the DRX mechanisms included CDRX, DDRX, GDRX, and twinning-induced DRX for the FSW joints. However, which DRX mechanism occurring in the joint depended on the temperature and strain rate [24].

During FSW/SFSW process, it is difficult to observe the temperature distribution and material flow behavior directly due to the severe plastic deformation coupled with high temperature and high strain rate in SZ. Therefore, the finite element simulation is suitable to explore the temperature and strain rate during FSW/SFSW process. Wu et al. [18] simulated the process of SFSW pure Ti using MSFESL software. They showed that the peak temperature of SFSW was ~ 687 °C, which was much lower than the β -transus temperature of Ti. In addition, the temperature increased gradually from base metal (BM) to SZ on the cross-sectional of the joint, and the temperatures of SZ and TMAZ reached 400–687 °C and 350–400 °C, respectively. Meanwhile, Singh et al. [21] obtained the temperature and strain distribution using Deform-3D software for the FSW pure Ti joints. The results illustrated that the peak temperature reached 820 °C in SZ, and the flow velocity and effective strain of the advancing side (AS) were higher than that of the retreating side (RS), which led to asymmetric microstructure and texture of AS and RS. Furthermore, Grujicic et al. [25] simulated the process of FSW TC4 alloy by ABAQUS software, showing that the effective strain of SZ was 20–50, and the effective strain was asymmetric due to the distinct material flow between AS and RS.

In summary, the complex flow of materials accompanied by DRX during the FSW/SFSW process, especially the high cooling rate of the water during the SFSW process will inevitably affect the DRX behavior. Therefore, it is necessary to clarify the effect of microstructure on the mechanical properties of SFSW Ti alloy joints. However, the study on SFSW Ti-15-3 alloy has not been reported until now, and the effect of forced cooling on microstructure evolutions and mechanical properties of the joint is not clear. In this work, the Ti-15-3 alloy joints were successfully prepared via SFSW for the first time. The grain refinement mechanisms and texture evolution behavior of the joints were analyzed according to the electron backscattered diffraction (EBSD) and finite element simulation. Finally, the strengthening mechanisms of the SFSW joint were revealed.

2 Experimental methods

2.1 Materials and methods

As-received forged Ti-15-3 alloy plates with a dimension of 120 mm \times 65 mm \times 3 mm were used in this study. The

single-pass SFSW was performed on a commercial friction stir welding equipment (FSW-LMAM16-2D) with a tool rotation speed of 250 rpm and a tool traverse speed of 50 mm/min. To avoid the welded defects, the stirring tool was tilted at an angle of 2° in a backward direction relative to the normal direction (ND). The stirring tool applied in this work was made of W–Re alloy and consisted of a concave shoulder with 12 mm in diameter and a conical pin with 2.5 mm in length and increasing diameters in the range of 3–6 mm. In the SFSW process, the forced cooling was carried out by the water with 25°C in a water tank (Fig. 1). During SFSW, a K-type thermocouple was used to measure the temperature in the SZ center.

The macrostructure of the cross-section of the SFSW joint was characterized by an optical microscope. The microstructure of the SFSW joint was analyzed using a scanning electron microscope (SEM, Gemini SEM 300) equipped with an OXFORD EBSD system. To observe the EBSD, the specimens were mechanically polished with abrasive paper and then electropolished to remove the residual stress on the surface. The electrolytic polishing was performed with 10% perchloric acid and 90% acetic acid, and the EBSD was conducted at a $0.11\ \mu\text{m}$ step and a 20 keV voltage. The inverse pole figure, polar figure, high and low angle grain boundaries, and dislocation density distribution were analyzed by Channel 5 software. Vickers microhardness was tested with an automatic microhardness tester (HXD-1000TM) at intervals of 0.5 mm on the cross-section of the joint, with a load of 200 g and a 15 s holding duration time. The tensile testing was conducted on a servohydraulic fatigue testing system (Instron 8801) at room temperature with an initial strain rate of $1.0 \times 10^{-3}\ \text{s}^{-1}$ according to the standard of GB/T 228.1-2010. Non-proportional tensile specimens were used to evaluate the tensile properties. The dog bone-shaped tensile specimens with a gauge dimension of $20 \times 4 \times 2\ \text{mm}^3$ and the local tensile specimens with a gauge dimension of $4 \times 2 \times 2\ \text{mm}^3$ were cut perpendicular to welding direction (WD). Each specimen was repeated at least three times to

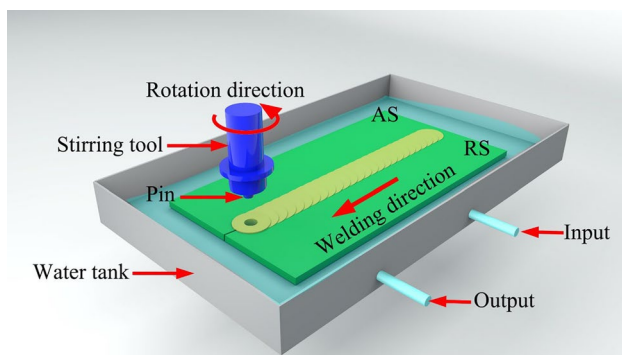


Fig. 1 Schematic diagram of SFSW

ensure the accuracy of the data. After the tensile test, the fracture surface was observed by SEM.

2.2 Finite element method

To analyze the temperature field, strain field, and material flow behavior during the SFSW process, the detailed evolutions of these characteristics were simulated by the commercial Deform-3D™ software. The stirring tool was considered to be a rigid part, and a constant value with a shear friction coefficient of 0.7 was used between the tool and the plate. A mesh window was adopted to refine the mesh in the tool path direction, while the rest of the workpiece maintained a coarse size. The minimum mesh size was 0.2 and 0.4 mm for the refined zone and undeformed zone, respectively, and the total number of hexagonal elements for the whole plate was $\sim 160,000$. The thermal convection coefficient of the Ti-15-3 alloy plate was $15\ \text{N/s/mm}^\circ\text{C}$, and the heat transfer coefficient between the tool and the Ti-15-3 alloy plate was $11\ \text{N/s/mm}^\circ\text{C}$. To ensure the accuracy of the simulation, the size of the stirring tool and welding parameters used in simulated were consistent with the experimental process.

3 Results

3.1 Microstructure

Figure 2 shows the microstructure and the pole figures (PFs) of BM. The black and white lines in EBSD images represent high-angle grain boundaries (HAGBs, $> 15^\circ$) and low-angle grain boundaries (LAGBs, $2^\circ\text{--}15^\circ$), respectively. Heterogeneous grain sizes were found in BM at an average of $\sim 650\ \mu\text{m}$. Meanwhile, it can be seen that a amount of LAGBs was distributed at the coarse grain boundaries with the proportion of 74%. Moreover, one can notice that the BM presented a pronounced grain orientation, which had been confirmed from a roughly-scanning EBSD mapping with the area of $8\ \text{mm}^2$ (not shown here).

Figure 3 shows the cross-section of the SFSW joint. There were no holes and cracks in SZ, indicating that the sound Ti-15-3 alloy joints were successfully prepared by SFSW. An obvious “basin-shaped” morphology appeared in SZ, and it almost symmetrical along the welding center, which implied a similar material flow behavior appeared on AS and RS.

To further study the microstructure evolutions of the joint during SFSW, the detailed microstructure on the TMAZ adjacent to RS (red rectangle in Fig. 3) was characterized in Fig. 4. Three significant regions were observed according to grain morphology. Region 1 was SZ, where fine equiaxed grains were uniformly distributed, with an average grain size of $1.5\ \mu\text{m}$. The zone adjacent to the BM

Fig. 2 **a** EBSD images and **b** corresponding (101) and (111) pole figures of BM

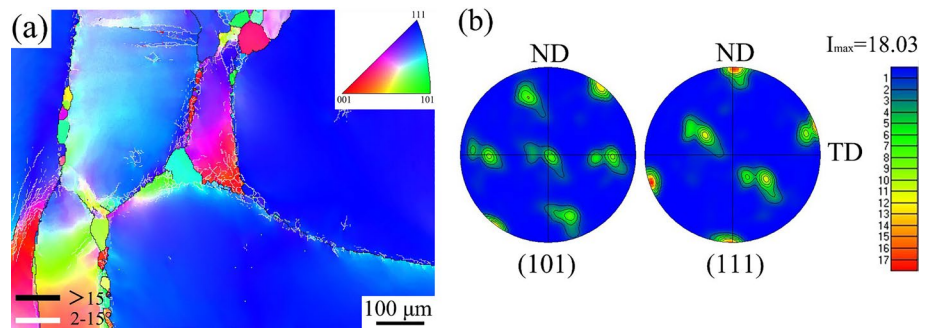


Fig. 3 Macrostructure of the SFSW joints

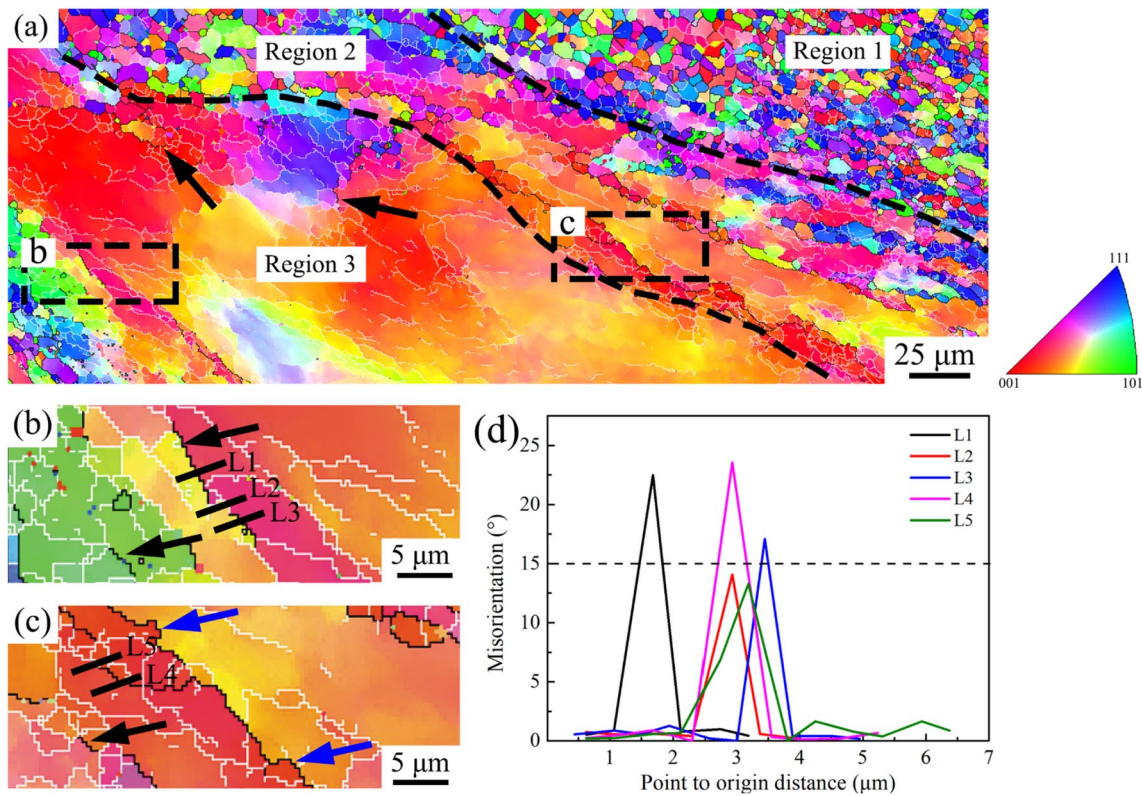


Fig. 4 **a** EBSD images of the TMAZ adjacent to the RS. **b, c** Magnifications of zones marked by the rectangles in **a**. **d** Misorientation angles versus distance along the lines marked in **b** and **c**

was the TMAZ, which could be divided into Region 2 and Region 3. In Region 2, the coarse grains were elongated with a large number of “chain-like” fine grains distributed around the coarse grain boundaries. This was because the Region 2 was subjected to severe shear and extrusion caused by the stirring tool, and the coarse grains were mechanically elongated. Hence the internal storage energy of the

deformed grains was increased, which promoted the DDRX, resulting in a large number of fine grains distributed around the elongated grains (blue arrows in Fig. 4c) [26]. This was because the low stacking fault energy of Ti-15-3 alloy contributed to DDRX. Different from Region 2, Region 3 retained some coarse grains, and a large number of fine grains appeared near the original coarse grains. Actually,

Region 2 and Region 3 were nearly composed of a coarse grain. During SFSW, the coarse grain suffered from severe deformation, which led to a large number of LAGBs aggregating inside the grains. The accumulated dislocations, as a result, increased the misorientation angles of the LAGBs and made them gradually transferred into HAGBs, as seen the discontinuous HAGBs noted by black arrows in Fig. 4a–c. This process was a typical CDRX [27]. Figure 4d shows the corresponding misorientation angle distribution of L1–L5 in Fig. 4b, c. The misorientation angles of L1, L3, and L4 were measured to be greater than 15° , and the misorientation angles of L2 and L5 were slightly less than 15° , which also demonstrated that LAGBs were transformed into HAGBs. It was noteworthy that the LAGBs were more likely to be aggregated at the original grain boundaries of coarse grains than the interior of the grains, and as a result, the occurrence of CDRX and grain refinement occurred preferentially and significantly at grain boundaries (Fig. 4b). This was attributed to the fact that when subjected to the shear of the tool, the dislocations inside the grains tended to slip and climb rapidly and then accumulated at the grain boundaries, which was benefit for the formation of LAGBs at the original grain boundaries of BM and induced the occurrence of CDRX. Therefore, CDRX and DDRX were the main DRX mechanisms in TMAZ.

To study the microstructure evolution of SZ, the different positions within SZ were characterized by EBSD, as

indicated in Fig. 5. It was evident that the fully fine and equiaxed grains were uniformly distributed at the top, middle, and bottom of SZ, while the grains were elongated at AS and RS. In addition, the LAGBs were evenly distributed in the SZ without noticeable aggregation, and the majority of the grains were segmented by LAGBs. Moreover, fine DRX grains appeared at the triple junction of grain boundaries in each zone (black rectangle in Fig. 5b–f). Meanwhile, the pronounced nucleation of subgrains appeared inside some grains (White rectangle in Fig. 5b–f). The above results indicated that three different CDRX behaviors occurred simultaneously in SZ during SFSW.

Furthermore, the proportion of LAGBs was more than 70% in BM and TMAZ, and significantly decreased to less than 40% in SZ. Especially the proportion of misorientation angle at the range of 4° – 13° in TMAZ was higher than in other zones (Fig. 6a), which was due to the low heat input and strain rate in TMAZ. During SFSW, the coarse grain in TMAZ was deformed and elongated, and then the dislocations were entangled and rapidly transformed into LAGBs. However, the low heat input and strain rate restrained the transformation, thus remaining a high proportion of LAGBs and high dislocation density in TMAZ (Fig. 6b, c). Moreover, a similar proportion of LAGBs in different positions of SZ indicated that the degree of CDRX in these positions was comparable (Fig. 6b). The similar geometric necessary dislocation density (GND) and grain size in each zone of SZ

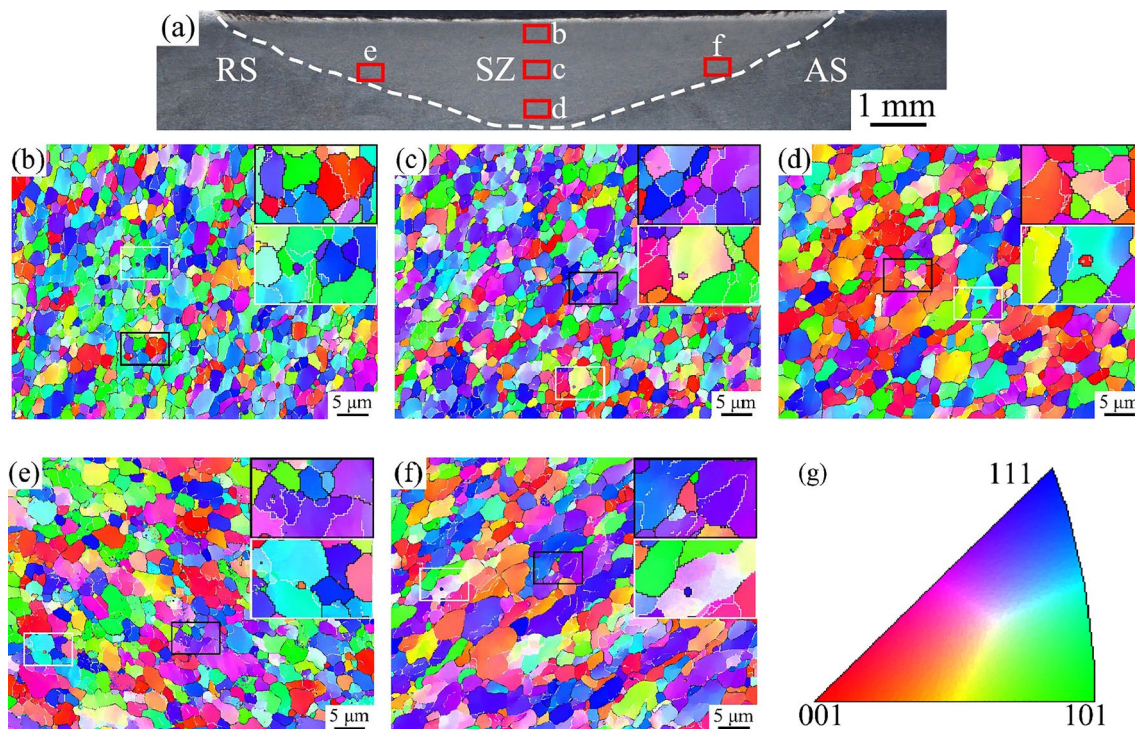
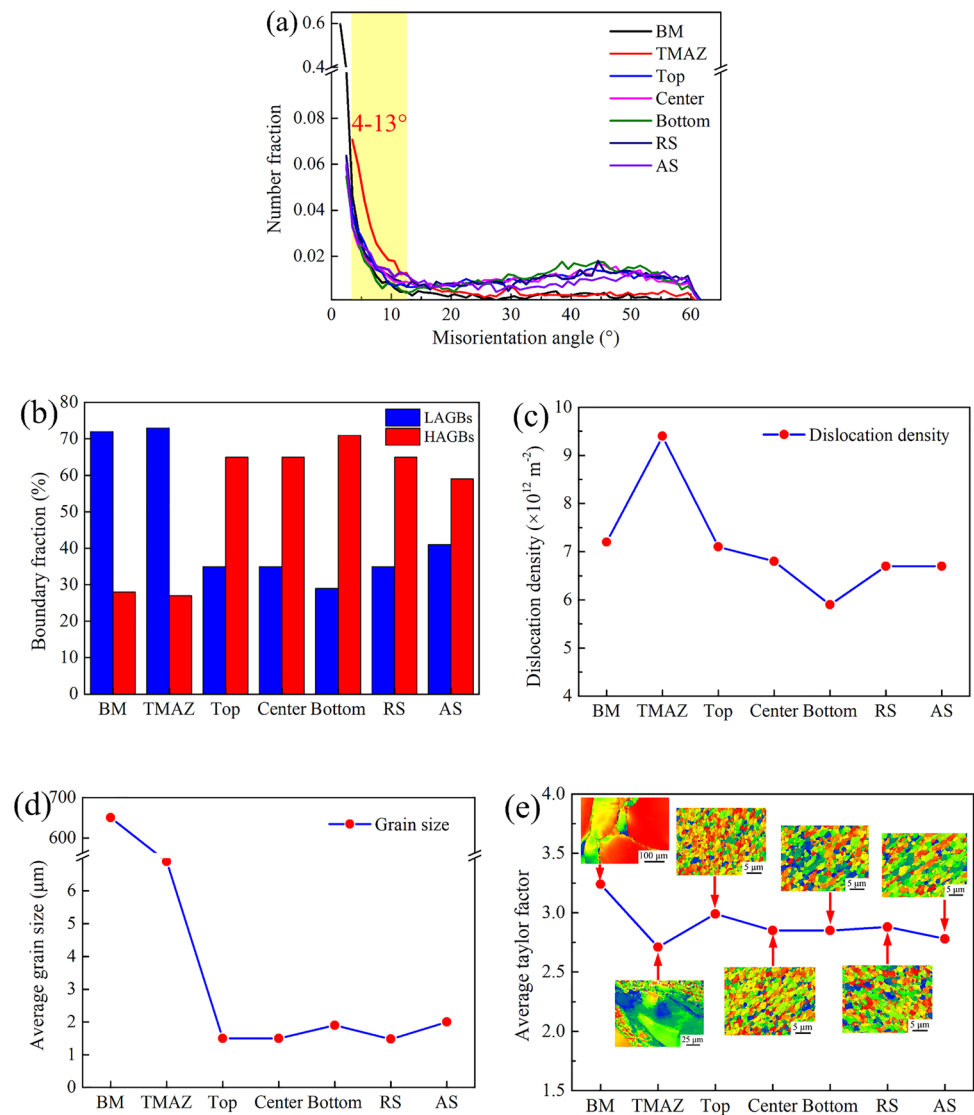


Fig. 5 a EBSD observations within the SZ; b–f EBSD images obtained from top, center, and bottom of SZ center, and RS and AS of SZ, respectively; g legend of EBSD images

Fig. 6 **a** Misorientation angles distribution; **b** Proportion of high angle and low angle boundaries; **c** dislocation density, **d** average grain size, and **e** average Taylor factors in different positions within FSW joints

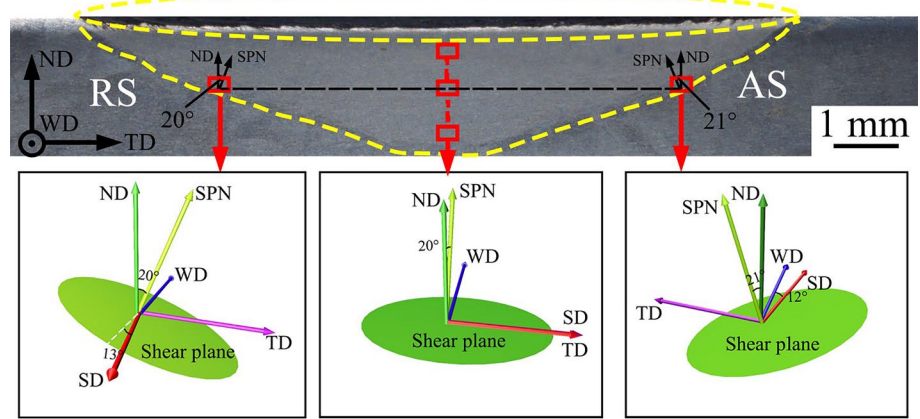


also confirmed the above results (Fig. 6c, d). Furthermore, the average Taylor factor was similar in each position of SZ, and it was slightly smaller than BM and larger than TMAZ (Fig. 6e). Compared with the BM, the grains were refined significantly due to the DRX during SFSW, decreasing from 650 μm to less than 10 μm (Figs. 2a and 6d). Particularly, the average grain size of SZ was even reduced to 2 μm , which was smaller than the Ti-15-3 alloy joints prepared by the conventional FSW in the air using the same parameters [23]. In summary, the fine and uniform microstructure of SZ can be achieved by SFSW.

It was reported that the material flow was extremely complicated in SZ during the SFSW, but it could be simplified to simple shear deformation [28]. Conventionally, the shear texture is defined in terms of the crystallographic plane $\{hkl\}$ and direction $\langle uvw \rangle$ parallel to the shear plane and shear direction (SD), respectively (Fig. 7). The corresponding polar figures have a reference frame where the shear

plane normal (SPN) is vertical and the SD is horizontal. It was reported that the shear plane within SZ was parallel with the surface of a truncated cone formed around the pin. Meanwhile, the diameter of the shear plane in the top and bottom of SZ was close to the diameter of the tool shoulder and the pin, respectively [29]. In this work, the angle between the SPN and ND was $\sim 21^\circ$ and $\sim 20^\circ$ on the AS/TMAZ border and RS/TMAZ border, respectively. Note that SD was generally considered to align with a circle of the horizontal section of the truncated cone. In light of this, the SD was parallel to transverse direction (TD) in SZ center and parallel with WD in the AS/TMAZ and RS/TMAZ borders. In fact, it was difficult to acquire the extremity positions of AS/TMAZ and RS/TMAZ borders. Hence tiny angles occurred between SD and WD in AS/TMAZ and RS/TMAZ borders. As shown in Fig. 7, the angles were $\sim 12^\circ$ and $\sim 13^\circ$ between SD and WD in the AS/TMAZ border and RS/TMAZ border, respectively.

Fig. 7 Schematic illustration of SPN and SD for each position within the SZ



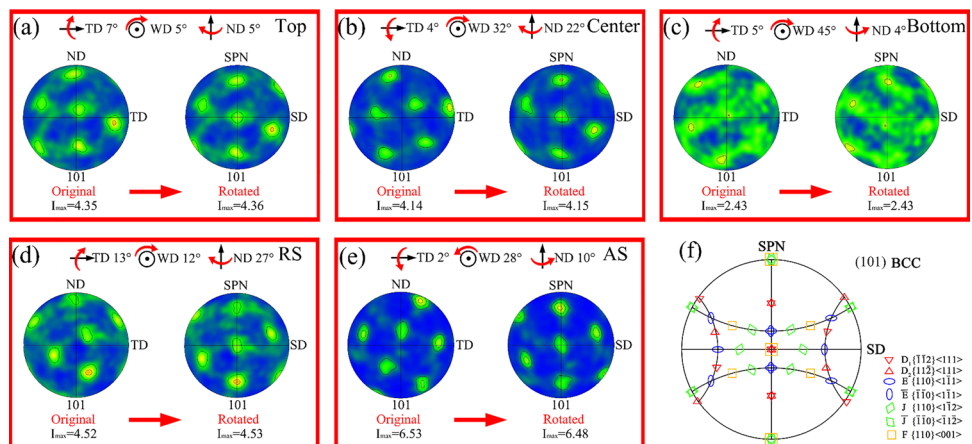
The texture evolution within SZ can be discussed by the corresponding (101) polar figures in Fig. 8. These polar figures have a reference frame in which the ND is vertical and the TD is horizontal, the same as that in the EBSD micrographs. Based on the abovementioned, the original (101) polar figures at the top, center, and bottom of SZ should rotate $\sim 20^\circ$ around TD to align the SPN with the conventional reference frame of simple shear texture. The rotated polar figures (not shown here) showed the characteristic poles close to but still slightly deviated from the ideal simple shear texture component of the BCC metals as Fig. 8f. Therefore, these polar figures needed to be further adjusted to well match the ideal simple shear texture (Fig. 8a–c). From the top to the bottom of the plate along the thickness direction, the rotation angles of the polar figures around WD gradually increased, indicating that the material flowed from the root of the pin to the top during the SFSW [30]. Similarly, the original (101) polar figures of the AS and RS needed to rotate $\sim 21^\circ$ and 20° around TD, and then rotate $\sim 12^\circ$ and $\sim 20^\circ$ around ND, respectively, to make the SPN vertical and the SD horizontal. Similar with the SZ center, the polar figures of RS and AS also needed to be further adjusted, as shown in Fig. 8d, e. The rotated polar figures

showed that all the examined positions in SZ were consistent with $\{110\} \langle uvw \rangle$ and $\{hkl\} \langle 111 \rangle$ ideal simple shear textures. The dominant shear texture component was $D_2(11\bar{2}) [111]$ in the top, center, and bottom of SZ center, while that of AS and RS was $D_1(\bar{1}1\bar{2}) [111]$. Mironov et al. [22] thought the predominant shear texture component was $J(\bar{1}10) [\bar{1}1\bar{2}]$ in SZ for the FSW Ti-15-3 joints, while Liu et al. [23] reported that the $D_2(11\bar{2}) [111]$ component was the main component in the whole SZ. These results were not match well the results of this study, which might be caused by the different SFSW parameters and the shape of the stirring pin [30]. It was worthwhile highlighting that the shear texture components of AS and RS were the same within SZ, which indicated the same material flow behavior on the AS and RS. This was because the SDs of AS and RS were almost parallel. The symmetry of the cross-sectional morphology along the SZ center in Fig. 3 also reflected this result.

3.2 Temperature, strain, and velocity simulation by finite element method

To explain the microstructure evolution behavior of the SFSW joint, the temperature, strain, and velocity of material

Fig. 8 a–e Original and final rotated (101) polar figures of top, center, and bottom of SZ-center, and RS and AS of SZ, respectively; f ideal simple shear texture components of BCC metals



flow were characterized by numerical simulation. It was recognized from temperature profile in Fig. 9a, b that the peak temperature reached 791–808 °C and distributed at the AS within SZ. Meanwhile, the temperature of the SZ dropped sharply due to the forced cooling of water, which was different from conventional FSW [31]. In TMAZ, the temperature was ~380 °C on RS, and it was slightly high on AS (~480 °C). This phenomenon was consistent with the result reported by Wu et al. [19]. At present, most previous

works analyzed the temperature field through a cross-section of the joint randomly. However, the welding speed actually can be divided into rotation speed component and the forward speed component, hence the temperature field was dynamically changed during the SFSW. In this work, point tracking method was used to capture the temperature at different positions of SZ. The distance between two adjacent points along ND and TD was 0.25 mm and 0.5 mm, respectively. The peak temperature distribution in SZ is shown

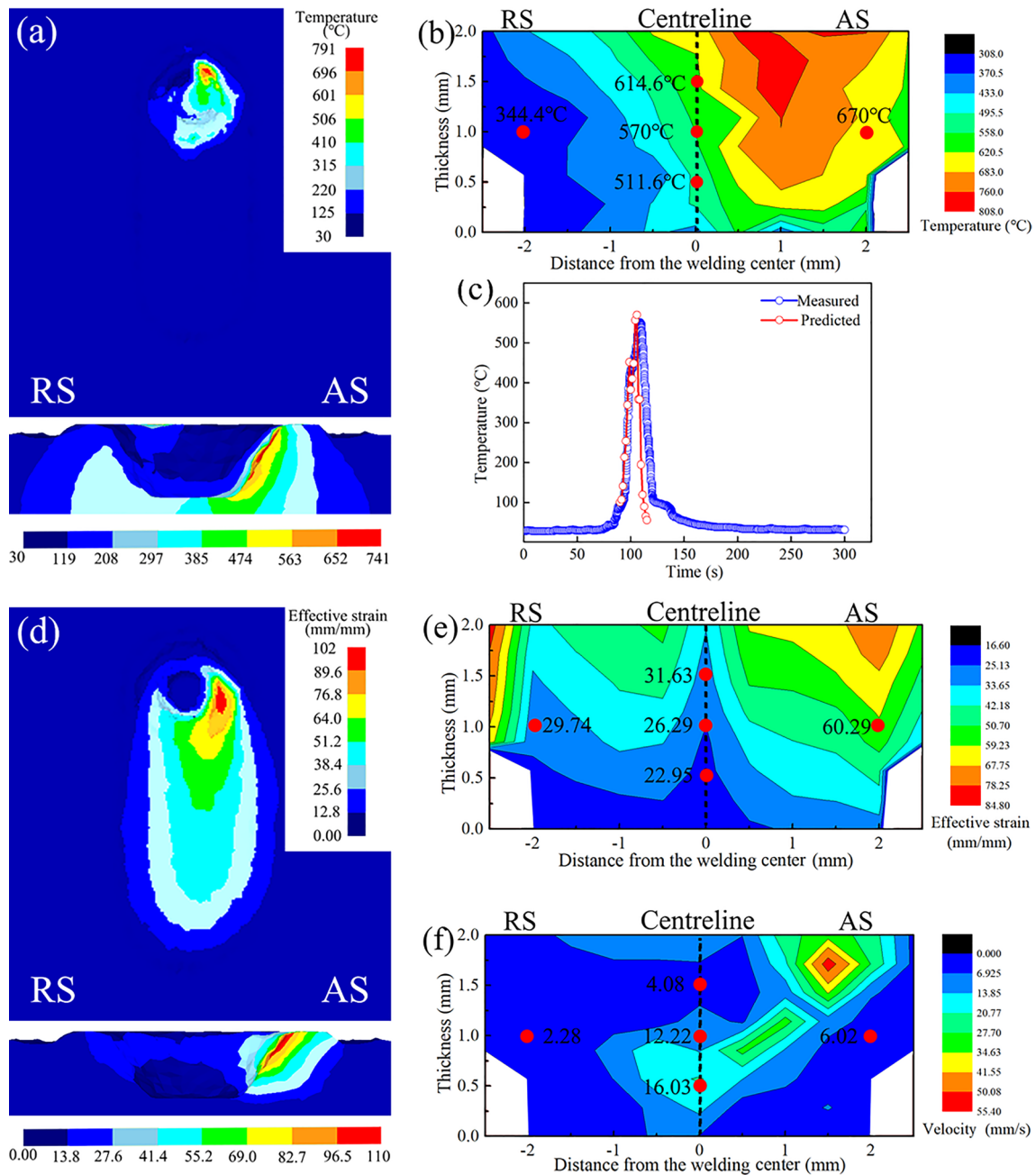


Fig. 9 Spatial distribution of **a, b** temperature for SFSW joint; **c** temperature curves of SZ center measured by K-type thermocouple and simulated by finite element method; Spatial distribution of **d, e** effective strain and **f** velocity for SFSW joint

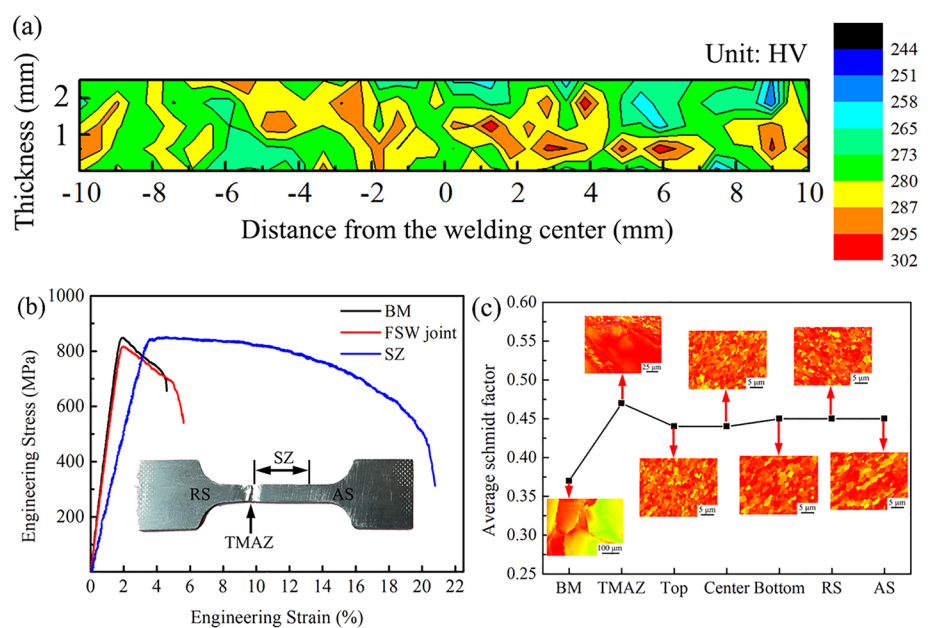
in Fig. 9b. It could be concluded that the peak temperature of SZ gradually decreased from the upper surface to the bottom of the plate, and the peak temperature on AS was higher than that of RS. In addition, the predicted temperature curve agreed well with the measured value, and the peak temperature ($\sim 550\text{ }^{\circ}\text{C}$) in the SZ center was lower than the β -transus temperature ($\sim 760\text{ }^{\circ}\text{C}$) of Ti-15-3 alloy (Fig. 9c). These results suggested that the simulated temperature field was reliable in this study. Similar to the temperature field distribution, the strain on the AS was higher than on the RS within SZ, and the maximum strain appeared at the AS near the upper surface of the plate (Fig. 9d, e). The strain also decreased gradually from the upper surface to the bottom of the plate, signifying that the displacement of the material at the tool root was larger than that at the tool tip. Singh et al. [21] also reported a similar result. To study the texture evolution behavior of SZ, the flow velocity of materials at different positions of SZ was characterized (Fig. 9f). The material flow velocity of AS was larger than RS, and the maximum velocity was $\sim 55\text{ mm/s}$, which appeared on the AS near the upper surface of the plate. This high material flow velocity made the strain rate reach 64 s^{-1} on SZ center, and the maximum strain rate reached $\sim 93\text{ s}^{-1}$ on the whole SZ (Supplementary 1). During the SFSW process, the material flowed rapidly in SZ and formed an ideal shear texture due to the coupled of high temperature and high strain rate of plastic deformation. Generally, a high temperature and strain would promote the DRX, thus lowering the texture intensity. In the present study, the degree of DRX in different positions of SZ was similar (Fig. 6a–d). Theoretically, the texture intensity was almost similar in the whole SZ. However, along the tool root to the tip, the temperature, strain, and texture intensity gradually decreased (Figs. 8 and 9).

This result indicated that the temperature and strain were proportional to the texture intensity when the temperature and strain exceeded the critical value required for DRX. In addition, the higher texture intensity of AS than RS also confirmed this result (Fig. 8). It was worth noting that the temperature of the top zone was much higher than RS in SZ, however, the strain and the texture intensity of the two positions was similar (Figs. 8 and 9e), which indicated that strain was the main factor determining the texture intensity. According to Fig. 9e, the strain on RS was higher than bottom zone in SZ, and the texture intensity of RS was also higher than bottom zone in SZ (Fig. 8c, d). Therefore, a high strain would improve the texture intensity. The detailed reason needs to be further investigated in the future work.

3.3 Mechanical properties

Figure 10a shows the distribution of microhardness along the TD-ND plane of the SFSW joint. There was no obvious softening zone in the whole joint, and the average microhardness distribution of SZ, TMAZ, and BM was uniform, which was 281 HV, 270 HV, and 279 HV, respectively. The average microhardness of SZ and TMAZ of the SFSW joint was higher than the Ti-15-3 joint prepared using conventional FSW by Liu et al. [23], which was mainly attributed to the fine-grained strengthening (Fig. 5). As the severe plastic deformation significantly refined the grain size of SZ during SFSW, according to the Hall–Petch relationship, the microhardness of SZ should be higher than that of BM in theory. However, a clear texture occurred in BM, which made up for the lack of fine-grained strengthening, triggering the similar microhardness values between BM and SZ.

Fig. 10 **a** Distribution of microhardness along the TD-ND plane; **b** engineering stress–strain curves; **c** average SF in each position of top, center, and bottom of SZ-center, and RS and AS of SZ, respectively



Generally speaking, the more uniform the microhardness distribution of SFSW joints, the better the coordinated deformation of each zone of the joint, and the optimal match of strength and plasticity for the entire joint. To evaluate the tensile properties of the SFSW joints, the engineering stress–strain curves of BM, SFSW joints, and SZ specimens were shown in Fig. 10b. The yield strength (YS), ultimate tensile strength (UTS), and elongation (EL) of BM were 829 MPa, 848 MPa, and 4.5%, respectively. The YS, UTS, and EL of SFSW joints were 800 MPa, 816 MPa, and 5.6%, respectively, reaching 96.5%, 96.2%, and 124% of BM. The SFSW joint failed at the RS of the TMAZ, mainly due to the strong soft orientation and the large grain size difference of the TMAZ (Figs. 3a and 10c). Generally, the TMAZ was limited and the tensile properties were difficult to evaluate. In this work, the SFSW joint fractured at the TMAZ, thus the tensile properties of the SFSW joint were equal to the tensile properties of the TMAZ. In addition, the tensile properties of SZ were also characterized (Fig. 11b). The YS, UTS, and EL of SZ reached 103%, 101%, and 467% of BM, respectively, mainly due to the fine-grained strengthening of SZ. Gupta et al. [32] reported that there was a relationship between UTS and Vickers microhardness: $UTS \text{ (MPa)} \approx 3 \times HV \text{ (Kgf/mm}^2\text{)}$ in aluminum matrix composite. In this work, the average microhardness distribution of SZ, TMAZ, and BM was 281 HV, 270 HV, and 279 HV, respectively. Therefore, the UTS of SZ, TMAZ, and BM was approximately 843 MPa, 810 MPa, and 837 MPa, which agreed well with the experimental values in Fig. 10b. Above results indicate that the relationship is also applicable to Ti-15-3 alloy. Recently, Wang et al. [33, 34] reported that the tensile strength of

solid-state welded joints is higher than that of fusion welding. In this work, the UTS of the SFSW joint was 11% higher than that of the joint welded by gas tungsten arc welding [1]. In summary, SFSW can prepare Ti-15-3 alloy joints with excellent performance and uniformity.

Figure 11 shows the tensile fracture morphology of BM, SFSW joint, and SZ specimens. A large number of dimples and a small number of micropores were distributed in the fracture surface of BM. The existence of micropores was because BM was forged insufficiently, so that a small number of as-cast defects were retained (Fig. 11a). Thereafter, these defects were easily prone to causing stress concentration during the tensile test, thus showing brittle fracture characteristics. Therefore, the fracture mechanism of BM was a ductile–brittle mixed fracture. Differently, the TMAZ and SZ specimens showed ductile fracture characteristics. The micropores in the fracture surface disappeared, and very fine dimples were distributed on the fractures. Note that the necking of SZ was more serious than that of TMAZ, and the distribution of dimples was more uniform. These results indicated that SZ had better plasticity than TMAZ. The results were consistent with the above engineering stress–strain curves.

4 Discussion

4.1 Microstructural evolution in TMAZ and SZ

Usually, temperature and strain rate are the dominant factors affecting DRX. The peak temperature and strain rate

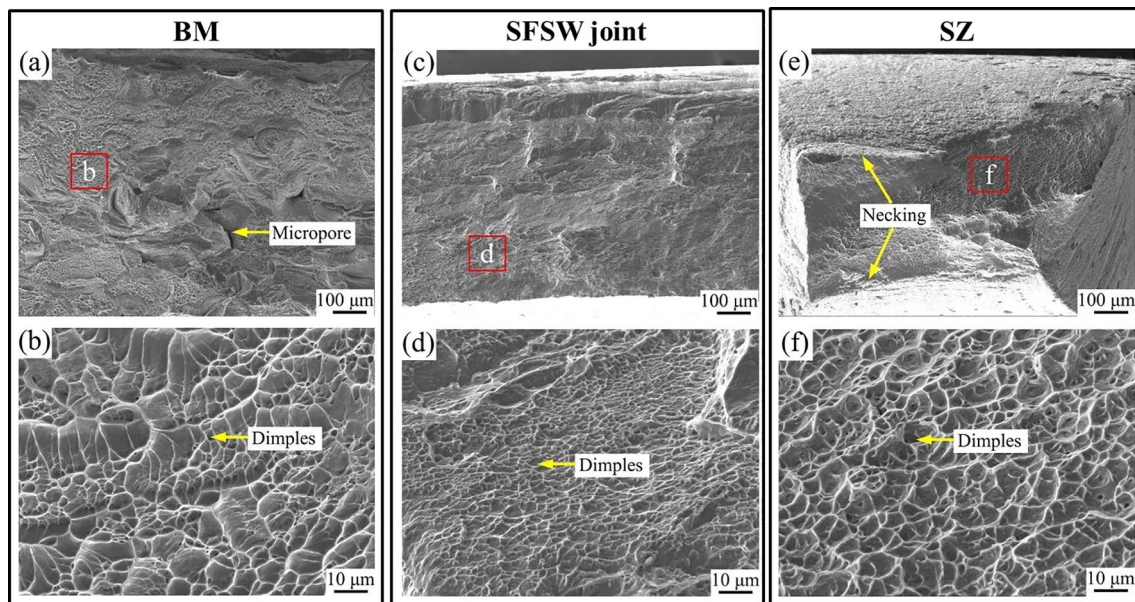


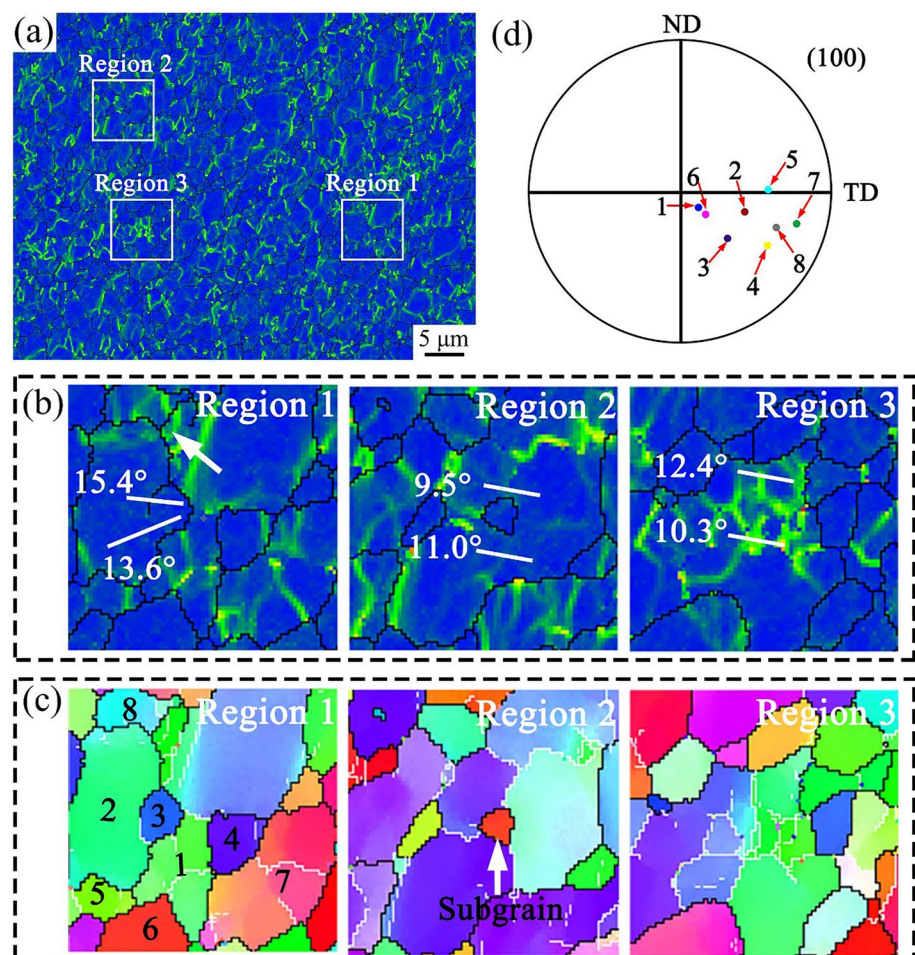
Fig. 11 Fracture surface of the a, b BM, c, d FSW joints, and e, f SZ

reached $\sim 550\text{ }^{\circ}\text{C}$ and $\sim 64\text{ s}^{-1}$ in the SZ center (Fig. 9c and Supplementary 1), respectively, which provided a positive condition for CDRX. Comparatively, a relatively low temperature ($380\text{--}480\text{ }^{\circ}\text{C}$) and strain rate ($\sim 10\text{ s}^{-1}$) occurred in TMAZ (Fig. 9a and Supplementary 1), thus the grains exhibited fiber elongated and equiaxed morphology, showing CDRX and DDRX characteristics (Fig. 4). Mironov et al. [22] and Liu et al. [23] pointed out that the DDRX was the main grain refinement mechanism in TMAZ due to the low stacking fault energy for Ti-15-3 alloy. This result was different from this work, which may be because the low heat input of SFSW weakened the mobility of dislocations, making dislocations accumulation and climbing to form discontinuous HAGBs, showing CDRX characteristics (Fig. 4). Note that both CDRX and DDRX have a grain refinement effect on the final microstructure.

In this work, three kinds of different CDRX behaviors occurred in SZ. (I) the severe plastic deformation caused by stirring tool broke the coarse grains, and the dislocations preferentially entangled at the triple-junction of grain boundaries through sliding and climbing to form LAGBs (white arrow in Fig. 12b). Subsequently, the LAGBs continuously

absorbed dislocations to increase the misorientation angle, which then transformed into HAGBs and formed equiaxed recrystallized grains. Note that the equiaxed recrystallized grains could separate the original grains by rotating (Region 1 in Fig. 12). However, Heidarzadeh et al. [35] believed that this behavior occurred through DDRX rather than CDRX. They reported that a pronounced strain gradient occurred due to the difference in storage energy between deformed grains and substructure grains, and the large strain gradient led the grains to migrate from low dislocation density toward high dislocation density, and the nucleus was separated by LAGBs. According to their point of view, the recrystallized Grain 3 of Region 1 in Fig. 12b belonged to the grain boundary migration process of Grain 2, and the migration direction towards Grain 1. However, the misorientation angle of Grain 3 increased significantly (Fig. 12b), and Grain 3 and Grain 2 exhibited different orientations in Fig. 12d, which indicated that the Grain 3 was not transformed by the grain boundary migration of Grain 2. In summary, the CDRX process (I) proposed in this study was reasonable. (II) When the coarse grains of BM were broken up by the stirring tool, dislocations were entangled in the grains to form LAGBs

Fig. 12 **a** Kernel average misorientation of the center in SZ; **b** the enlarged rectangle in **a** and **c** the corresponding inverse polar figure; **d** the polar figure in the Region 1 in **c**



and transformed into HAGBs through dynamic recovery. As the misorientation angle of HAGBs gradually increased, the subgrains were formed. Finally, the original grains were divided by the rotation of subgrains (Region 2 in Fig. 12). Similar results were obtained by Singh et al. [21]. (III) The LAGBs formed in the SFSW process directly divided the original grains, and then the LAGBs gradually transformed into discontinuous HAGBs by absorbing the dislocations. Subsequently, these discontinuous HAGBs aggregated to form fine equiaxed DRX grains (Region 3 in Fig. 12). It was worth noting that when the LAGBs divided the grains in process (III), they might be transformed into subgrains, and refined the grains through process (II).

Kim et al. [20] and Singh et al. [21] showed that the main grain refinement mechanisms in SZ were CDRX and DDRX during FSW pure Ti/TC4 alloy process. Usually, CDRX appeared in the early stage of deformation, while DDRX required large strain and sufficient high heat input, therefore, it usually occurred in the late stage of deformation. In this work, the forced cooling effect of water caused the temperature to drop rapidly in SZ (Fig. 9a), which could not provide sufficient heat input for DRX. Therefore, the grain refinement mechanism was CDRX in SZ. In addition, the Taylor factor can be utilized to discuss the DRX behaviors. A zone with a relatively high level of the Taylor factor was less likely to nucleate via a DDRX because sufficient restoration in the grain was required to initiate mobility for the HAGBs [16]. Xie et al. [36] reported that a minimum value of the Taylor factor was essential for the nucleation of new grains via DDRX, but at the same time, the value should not exceed the threshold limit. For the AZ31 Mg alloys, the threshold limit value was 3.1 during hot compression testing. In this work, the average Taylor factors were similar at different positions within SZ, and these values were slightly smaller than that of BM (3.24) but slightly larger than that of TMAZ (2.71) (Fig. 6e). Moreover, the CDRX occurred in SZ, while the CDRX and DDRX occurred in TMAZ. Therefore, the threshold limit value of the average Taylor factor for occurring DDRX of Ti-15-3 alloy was between 2.71 and 2.78.

4.2 Relationship between microstructure and mechanical properties of the joint

The peak temperature in the SZ center was ~ 550 °C, which was significantly lower than the β -transus temperature of Ti-15-3 alloy (~ 760 °C). This result was in good accordance the microstructure, where no lamellar $\alpha + \beta$ phase in Fig. 5. For the SFSW joint, the main factors affecting its mechanical properties were fine-grained strengthening, strain strengthening, and texture strengthening. At present, the classical Hall–Petch relationship was a wide method for describing the relationship between YS and grain size of metals.

Recently, Jiang et al. [37] established a novel Hall–Petch relationship according to a data-driven machine learning method. The model is shown in Eq. (1).

$$\sigma_y = 79W/(S^3 \sqrt{l_t}) + 1.2\sqrt{\gamma E/l_t}d^{-0.5} \quad (1)$$

where σ_y is the YS, W is cohesive energy (~ 8.5 eV [38]), S is valence electron distance (~ 1.61 nm [39]), l_t is the linear thermal expansion ($l_t = \frac{1}{2}Gb^2$), G is the shear modulus (~ 23.8 GPa [40]), b is the burgers vector (~ 0.28 nm), γ is the grain boundary interface energy (~ 990 mJ/m² [41]), E is Young's modulus (~ 77 GPa [42]), and d is the average grain size. According to Eq. (1), the contribution of grain size to YS is 180 MPa, 297 MPa, and 446 MPa, respectively, for BM, TMAZ, and SZ. Therefore, the order of fine grain strengthening of the SFSW joint is: BM < TMAZ < SZ.

Usually, dislocation strengthening included GND strengthening and statistical storage dislocation strengthening. Cui et al. [43] found that GND strengthening accounted for more than 90% of dislocation strengthening, which indicated that GND strengthening played a leading role in the SFSW joint. Zhu et al. [44] also confirmed the results. The strength increment ($\Delta\sigma_{GND}$) caused by GND can be calculated by Eq. (2).

$$\Delta\sigma_{GND} = M\alpha Gb\rho^{1/2} \quad (2)$$

where M is the Taylor factor, and α is a constant (It is related to dislocation structure. Here the value is 0.23). The dislocation density (ρ) was calculated by the average misorientations angles according to Eq. (3).

$$\rho = \frac{2\theta_{av}}{\mu b} \quad (3)$$

where θ_{av} represents the average misorientations, and μ is the step size. The GND density was similar for different positions within SZ, which indicated a uniform DRX occurred in SZ (Fig. 6c). The similar HAGBs proportions and grain sizes also proved to this result (Fig. 6b, d). According to Eq. (2), the contribution of GND to YS is 133 MPa, 127 MPa, and 114 MPa, respectively, for BM, TMAZ, and SZ. Hence the order of GND strengthening of the SFSW joint is: SZ < BM < TMAZ.

Last, the texture strengthening (σ_t) can be determined according to Eq. (4).

$$\sigma_t = \frac{\tau_0}{m} \quad (4)$$

where τ_0 is the critical shear stress (~ 129 MPa [45]), and m is the Schmidt factor. The contribution of texture intensity to YS is 349 MPa, 275 MPa, and 293 MPa, respectively, for BM, TMAZ, and SZ. The order of GND strengthening of the SFSW joint is: TMAZ < SZ < BM.

Although the contributions of various strengthening mechanisms in different zones were different for the SFSW joint, the main strengthening mechanism of TMAZ and SZ was fine-grained strengthening. In addition, the calculated values (662 MPa and 699 MPa) of BM and TMAZ were smaller than the measured values (829 MPa and 800 MPa), while the calculated strength (854 MPa) of SZ was almost the same as the measured value (853 MPa). This was because the large difference in the grain size distribution increased the calculated errors in BM and TMAZ [46]. In summary, the YS and UTS of the BM, TMAZ, and SZ were relatively similar, which indicated it was an effective method to prepare a uniform and high-performance Ti-15-3 alloy joint through SFSW.

5 Conclusion

In this work, the Ti-15-3 alloy joints were successfully prepared via SFSW. The detailed microstructure evolution and mechanical properties of the SFSW joints were studied according to the experimental results and finite element simulation. The main conclusions are as follows:

- (1) During SFSW, the peak temperature of TMAZ and SZ reached ~ 480 °C and ~ 808 °C, and the maximum strain rate reached ~ 10 s⁻¹ and ~ 93 s⁻¹, respectively. The high temperature and large strain rate promoted the DRX, which refined the grain size of TMAZ and SZ to less than 10 μ m. The main grain refinement mechanism of TMAZ was CDRX and DDRX, while that of SZ was CDRX. The threshold limit value of the average Taylor factor for occurring DDRX of Ti-15-3 alloy was between 2.71 and 2.78.
- (2) The complex materials flow of SZ could be simplified as ideal shear deformation during SFSW. The shear textures components at the top, center, and bottom of SZ were $D_2(1\bar{1}\bar{2})[111]$, while that of AS and RS within SZ was $D_1(1\bar{1}\bar{2})[111]$. The same shear texture components at AS and RS within SZ indicated the same material flow behavior occurred at these two positions. Furthermore, a large strain would be conducive to improving the texture intensity.
- (3) A relative uniform microhardness distribution was observed across the SFSW joint, and the average microhardness value was 281 HV, 270 HV, and 279 HV in SZ, TMAZ, and BM, respectively. The YS, UTS, and EL of the SFSW joint were 800 MPa, 816 MPa, and 5.6%, reaching that of 96.5%, 96.2%, and 124% of BM, respectively. Meanwhile, the YS, UTS, and EL in SZ reached 103%, 101%, and 467% of BM. Note that the UTS and microhardness of each zone of the SFSW joint

meet the following relationship: UTS (MPa) $\approx 3 \times HV$ (Kgf/mm²).

Supplementary Information The online version contains supplementary material available at <https://doi.org/10.1007/s43452-024-00877-x>.

Acknowledgements The authors gratefully acknowledge China's National Defense Science and Technology (173 Program) [2021-JCJQ-JJ-0190], the National Natural Science Foundation of China (Major Scientific Research Instruments) [52227807], the National Natural Science Foundation of China [Nos. 52104383, 52034005], the Shaanxi Province National Science Fund for Distinguished Young Scholars [2022JC-24], the Key Research and Development Project of Shaanxi Province (2022JBGS2-01), and the Scientific Research Program for Youth Innovation Team Construction Project of Department Education of Shaanxi Provincial (21JP058).

Data availability Data will be made available on request.

Declarations

Conflict of interest The authors declare they have no financial interests.

Ethics approval Written informed consent for publication of this paper was obtained from the Xi'an University of Architecture and Technology and all authors.

References

1. Anis AL, Talari MK, Babu NK, et al. Grain refinement of Ti-15V-3Cr-3Sn-3Al metastable β titanium alloy welds using boron-modified fillers. *J Alloys Compd.* 2018;749:320–8. <https://doi.org/10.1016/j.jallcom.2018.03.286>.
2. Sarkar R, Ghosal P, Muraleedharan K, et al. Effect of boron and carbon addition on microstructure and mechanical properties of Ti-15-3 alloy. *Mater Sci Eng A.* 2018;528:4819–29. <https://doi.org/10.1016/j.msea.2011.03.014>.
3. Balachandar K, Sarma VS, Pant B. Microstructure and mechanical properties of gas-tungsten-arc-welded Ti-15-3 beta titanium alloy. *Mater Sci Eng A.* 2009;40:2685–93. <https://doi.org/10.1007/s11661-009-9952-8>.
4. Zhang BG, Wang T, Duan XH, et al. Temperature and stress fields in electron beam welded Ti-15-3 alloy to 304 stainless steel joint with copper interlayer sheet. *Trans Nonferr Metal Soc.* 2012;22:398–403. [https://doi.org/10.1016/S1003-6326\(11\)61190-4](https://doi.org/10.1016/S1003-6326(11)61190-4).
5. Beygi R, Galvão I, Akhavan-Safar A, et al. Effect of alloying elements on intermetallic formation during friction stir welding of dissimilar metals: a critical review on aluminum/steel. *Metal.* 2023;13:768. <https://doi.org/10.3390/met13040768>.
6. Wang W, Han P, Peng P, et al. Friction stir processing of magnesium alloys: a review. *Acta Metall Sin-Engl.* 2020;33:43–57. <https://doi.org/10.1007/s40195-019-00971-7>.
7. Pouraliakbar H, Beygi R, Fallah V, et al. Processing of Al-Cu-Mg alloy by FSSP: Parametric analysis and the effect of cooling environment on microstructure evolution. *Mater Lett.* 2022;308:131157. <https://doi.org/10.1016/j.matlet.2021.131157>.
8. Qiao K, Wang KS, Wang J, et al. Microstructural evolution and deformation behavior of friction stir welded twin-induced

- plasticity steel. *J Mater Sci Technol.* 2024;169:68–81. <https://doi.org/10.1016/j.jmst.2023.05.053>.
9. Ishida K, Gao Y, Nagatsuka K, et al. Microstructures and mechanical properties of friction stir welded lap joints of commercially pure titanium and 304 stainless steel. *J Alloys Compd.* 2015;630:172–7. <https://doi.org/10.1016/j.jallcom.2015.01.004>.
 10. Wang W, Han P, Yuan J, et al. Enhanced mechanical properties of pure zirconium via friction stir processing. *Acta Metall Sin-Engl.* 2020;33:147–53. <https://doi.org/10.1007/s40195-019-00939-7>.
 11. Pouraliakbar H, Aval HJ, Howells A, et al. Microstructural evolution and mechanical properties of rapidly solidified thin-strip continuous cast AA5182 Al-Mg alloy under varying heat inputs in friction stir welding. *Int J Adv Manuf Technol.* 2023;129:2921–31. <https://doi.org/10.1007/s00170-023-12505-8>.
 12. Zhang Y, Sato YS, Kokawa H, et al. Microstructural characteristics and mechanical properties of Ti-6Al-4V friction stir welds. *Mater Sci Eng A.* 2008;485:448–55. <https://doi.org/10.1016/j.msea.2007.08.051>.
 13. Kitamura K, Fujii H, Iwata Y, et al. Flexible control of the microstructure and mechanical properties of friction stir welded Ti-6Al-4V joints. *Mater Des.* 2013;46:348–54. <https://doi.org/10.1016/j.matdes.2012.10.051>.
 14. Su JQ, Wang JY, Mishra RS, et al. Microstructure and mechanical properties of a friction stir processed Ti-6Al-4V alloy. *Mater Sci Eng A.* 2013;573:67–74. <https://doi.org/10.1016/j.msea.2013.02.025>.
 15. Feng XL, Liu HJ, Lippold JC. Microstructure characterization of the stir zone of submerged friction stir processed aluminum alloy 2219. *Mater Charact.* 2013;177:97–102. <https://doi.org/10.1016/j.matchar.2013.05.010>.
 16. Liu HH, Ushida K, Fujii H. Elucidation of microstructural evolution of beta-type titanium alloy joint during friction stir welding using liquid CO₂ cooling. *Mater Charact.* 2018;145:490–500. <https://doi.org/10.1016/j.matchar.2018.09.005>.
 17. Cao FJ, Sun T, Hu JP, et al. Enhanced mechanical and anticorrosion properties in cryogenic friction stir processed duplex stainless steel. *Mater Des.* 2022;225: 111492. <https://doi.org/10.1016/j.matdes.2022.111492>.
 18. Wu LH, Zhang H, Zeng XH, et al. Achieving superior low temperature and high strain rate superplasticity in submerged friction stir welded Ti-6Al-4V alloy. *Sci China Mater.* 2018;61:417–23. <https://doi.org/10.1007/s40843-017-9145-4>.
 19. Wu LH, Hu XB, Zhang XX, et al. Fabrication of high-quality Ti joint with ultrafine grains using submerged friction stirring technology and its microstructural evolution mechanism. *Acta Mater.* 2019;166:371–85. <https://doi.org/10.1016/j.actamat.2018.12.059>.
 20. Kim JD, Murugan SP, Kim JW, et al. α/β phase transformation and dynamic recrystallization induced microstructure development in fine-grained Ti-6Al-4V friction stir weld. *Mater Charact.* 2021;178: 111300. <https://doi.org/10.1016/j.matchar.2021.111300>.
 21. Singh AK, Kaushik L, Singh J, et al. Evolution of microstructure and texture in the stir zone of commercially pure titanium during friction stir processing. *Int J Plast.* 2022;150: 103184. <https://doi.org/10.1016/j.ijplas.2021.103184>.
 22. Mironov S, Sato YS, Kokawa H. Microstructural evolution during friction stir welding of Ti-15V-3Cr-3Al-3Sn alloy. *Mater Sci Eng A.* 2010;527:7498–504. <https://doi.org/10.1016/j.msea.2010.08.074>.
 23. Liu H, Fujii H. Microstructural and mechanical properties of a beta-type titanium alloy joint fabricated by friction stir welding. *Mater Sci Eng A.* 2018;527:140–8. <https://doi.org/10.1016/j.msea.2017.11.006>.
 24. Pierce DT, Jimenez JA, Bentley J, et al. The influence of stacking fault energy on the microstructural and strain hardening evolution of Fe-Mn-Al-Si steels during tensile deformation. *Acta Mater.* 2015;100:178–90. <https://doi.org/10.1016/j.actamat.2015.08.030>.
 25. Grujicic M, Arakere G, Pandurangan B, et al. Computational analysis and experimental validation of the friction-stir welding behaviour of Ti-6Al-4V. *P I Mech Eng B-J Eng.* 2011;225:208–23. <https://doi.org/10.1177/09544054JEM2013>.
 26. Peng P, Wang KS, Wang W, et al. Relationship between microstructure and mechanical properties of friction stir processed AISI 316L steel produced by selective laser melting. *Mater Charact.* 2021;163: 110283. <https://doi.org/10.1016/j.matchar.2020.110283>.
 27. Han P, Wang W, Liu ZH, et al. Modification of cold-sprayed high-entropy alloy particles reinforced aluminum matrix composites via friction stir processing. *J Alloys Compd.* 2022;907: 164426. <https://doi.org/10.1016/j.jallcom.2022.164426>.
 28. Yoon S, Ueji R, Fujii H. Microstructure and texture distribution of Ti-6Al-4V alloy joints friction stir welded below β -transus temperature. *J Mater Process Technol.* 2016;22:390–7. <https://doi.org/10.1016/j.jmatprotec.2015.09.041>.
 29. Reynolds AP, Hood E, Tang W. Texture in friction stir welds of Timental 21S. *Scr Mater.* 2005;52:491–4. <https://doi.org/10.1016/j.scriptamat.2004.11.009>.
 30. Jain R, Pal SK, Singh SB. Finite element simulation of pin shape influence on material flow, forces in friction stir welding. *Int J Adv Manuf Technol.* 2018;94:1781–97. <https://doi.org/10.1007/s00170-017-0215-3>.
 31. Hassanamraji N, Eivani AR, Aboutalebi MR. Finite element simulation of deformation and heat transfer during friction stir processing of as-cast AZ91 magnesium alloy. *J Mater Res Technol.* 2021;17:2998–3017. <https://doi.org/10.1016/j.jmrt.2021.08.087>.
 32. Gupta M, Srivatsan TS. Interrelationship between matrix microhardness and ultimate tensile strength of discontinuous particulate-reinforced aluminum alloy composites. *Mater Lett.* 2001;51:255–61. [https://doi.org/10.1016/S0167-577X\(01\)00300-7](https://doi.org/10.1016/S0167-577X(01)00300-7).
 33. Wang SL, Zhou BB, Zhang X, et al. Mechanical properties and interfacial microstructures of magnetic pulse welding joints with aluminum to zinc-coated steel. *Mater Sci Eng A.* 2020;788: 139425. <https://doi.org/10.1016/j.msea.2020.139425>.
 34. Wang SL, Xu LW, Sun T, et al. Effects of process parameters on mechanical performance and interfacial morphology of electromagnetic pulse welded joints between aluminum and galvanized steel. *J Mater Res Technol.* 2021;10:552–64. <https://doi.org/10.1016/j.jmrt.2020.12.047>.
 35. Heidarzadeh A, Mironov S, Kaibyshev R, et al. Friction stir welding/processing of metals and alloys: a comprehensive review on microstructural evolution. *Prog Mater Sci.* 2021;117: 100752. <https://doi.org/10.1016/j.pmatsci.2020.100752>.
 36. Xie C, He JM, Zhu BW, et al. Transition of dynamic recrystallization mechanisms of as-cast AZ31 Mg alloys during hot compression. *Int J Plast.* 2018;111:211–33. <https://doi.org/10.1016/j.ijplas.2018.07.017>.
 37. Jiang L, Fu HD, Zhang HT, et al. Physical mechanism interpretation of polycrystalline metals' yield strength via a data-driven method: a novel Hall–Petch relationship. *Acta Mater.* 2022;231: 117868. <https://doi.org/10.1016/j.actamat.2022.117868>.
 38. Peng Y, Zhu QQ, Guo YH, et al. Effects of alloying elements on the stability and mechanical properties of β -Ti0.5X0.5 (X = V, Cr, Mn, Fe; Nb, Mo, Tc, Ru; Ta, W, Re, Os) alloys according to first-principles calculations. *Solid State Commun.* 2021;334: 114395. <https://doi.org/10.1016/j.ssc.2021.114395>.
 39. Qi L, He SY, Chen CJ, et al. Diffusional-displacive transformation in a metastable b titanium alloy and its strengthening effect. *Acta Mater.* 2020;195:151–62. <https://doi.org/10.1016/j.actamat.2020.05.058>.

40. Ledbetter H, Ogi H, Kai S, et al. Elastic constants of body centered-cubic titanium monocrystals. *J Appl Phys.* 2004;95:4642–4. <https://doi.org/10.1063/1.1688445>.
41. Chen W, Zhang JY, Cao S, et al. Strong deformation anisotropies of ω -precipitates and strengthening mechanisms in Ti-10V-2Fe-3Al alloy micropillars: precipitates shearing vs precipitates disordering. *Acta Mater.* 2016;117:68–80. <https://doi.org/10.1016/j.actamat.2016.06.065>.
42. Shitara K, Yokota K, Yoshiya M, et al. Ples design and experimental validation of β -Ti alloys with high solid-solution strengthening and low elasticities. *Mater Sci Eng A.* 2022;843: 143053. <https://doi.org/10.1016/j.msea.2022.143053>.
43. Cui LQ, Jiang S, Xu JH, et al. Revealing relationships between microstructure and hardening nature of additively manufactured 316L stainless steel. *Mater Des.* 2021;198: 109385. <https://doi.org/10.1016/j.matdes.2020.109385>.
44. Zhu JM, Wu HH, Wang D, et al. Crystallographic analysis and phase field simulation of transformation plasticity in a multifunctional β -Ti alloy. *Int J Plast.* 2017;189:110–29. <https://doi.org/10.1016/j.ijplas.2016.11.006>.
45. Ojha A, Sehitoglu H. Critical stresses for twinning, slip, and transformation in Ti-based shape memory alloys. *Shap Mem Superelasticity.* 2016;2:180–95. <https://doi.org/10.1007/s40830-016-0061-4>.
46. Lu L, Chen X, Huang X, et al. Revealing the maximum strength in nanotwinned copper. *Science.* 2009;323:607–10. <https://doi.org/10.1126/science.1167641>.

Publisher's Note Springer Nature remains neutral with regard to jurisdictional claims in published maps and institutional affiliations.

Springer Nature or its licensor (e.g. a society or other partner) holds exclusive rights to this article under a publishing agreement with the author(s) or other rightsholder(s); author self-archiving of the accepted manuscript version of this article is solely governed by the terms of such publishing agreement and applicable law.